RSC Advances

ROYAL SOCIETY OF **CHEMISTRY**

www.rsc.org/advances

Journal Name

ARTICLE

Additive-free 1,4-butanediol mediated synthesis: a suitable route to obtain nanostructured, mesoporous spherical zinc oxide materials with multifunctional properties

Diana Visinescu,[a*] Mariana Scurtu,[a] Raluca Negrea,[b] Ruxandra Birjega,[c] Daniela C. Culita,[a] Mariana Carmen Chifiriuc,[d] Constantin Draghici,[e] Jose Calderon Moreno,[a] Adina Magdalena Musuc,[a] Ioan Balint[a] and Oana Carp[a*]

A family of mesoporous, self-aggregated zinc oxide materials with spherical morphologies of high crystalline quality, is obtained through a facile, additive-free polyol procedure. The forced hydrolysis of zinc acetylacetonate in 1,4-butanediol (BD), in various reaction conditions, affords ZnO materials with versatile morphologies and optical properties. The reaction parameters (temperature, time and zinc source concentration) modulate the ZnO nanocrystallites size (from 8.1 to 13.2 nm), the spheres diameter (ranging from 50 up to 250 nm), the internal structure of the spherical aggregates (hollow or solid) and their specific surface area (from 31 to 92 m^2/g). Polycrystalline spheres with hollow cores are obtained at the lowest temperature (90°C) and zinc cation concentration (0.1 M), while at higher reaction temperatures (140-180°C), solid spherical aggregates are developed. A reaction mechanism for ZnO formation via zinc layered hydroxide (LDH-Zn) is proposed based on the nuclear magnetic resonance (^{1}H NMR and ^{13}C NMR) and powder X-ray diffraction (XRD) studies. The obtained ZnO materials have a functionalized surface, derived from the polyol solution and act as nitrogen selective photocatalyst in the reduction reaction of NO_3^-. The organic residua attached on the ZnO surface play a crucial role in the denitrification reaction, since the photo-cleaned sample showed a negligible photocatalytic activity. The ZnO materials also exhibited microbicidal and anti-biofilm activity against reference and clinical strains, highlighting their potential for the development of novel antimicrobial formulation.

Introduction

Zinc oxide (ZnO) is a multifunctional oxide-based material with an extraordinary technical potential due to a unique

[a.] "Ilie Murgulescu" Institute of Physical Chemistry, Romanian Academy, 202 Splaiul Independentei, 060021 Bucharest, Romania. E-mail: ocarp@icf.ro, diana.visinescu@gmail.com
[b.] National Institute of Materials Physics, Atomistilor 105bis, 77125, Magurele, Ilfov, Romania
[c.] National Institute for Lasers, Plasma and Radiation Physics, 409 Atomistilor, PO-Box MG-36, 077125 Bucharest, Romania.
[d.] University of Bucharest, Faculty of Biology, Microbiology Department, 1–3 Portocalilor Way, Bucharest, Romania.
[e.] Organic Chemistry Center "C.D.Nenitescu", 202 B Splaiul Independentei, Bucharest 060023, Romania

† Electronic Supplementary Information (ESI) available: thermal curves for Zn(acac)$_2$·1.2H$_2$O (Fig. S1), FTIR spectra for **ZnO$_{BD1}$-ZnO$_{BD3}$** (Fig. S2), **ZnO$_{BD4}$, ZnO$_{BD5}$** (Fig. S3) and for **ZnO$_{BD6}$, ZnO$_{BD7}$** (Fig. S4), ^{1}H NMR and ^{13}C NMR spectra for **ZnO$_{BD2}$** (Fig. S5) and **ZnO$_{BD7}$** (Fig. S6), thermal curves for **ZnO$_{BD7}$** oxide (Fig. S7), XRD diffractograms for **ZnO$_{BD4}$-ZnO$_{BD7}$** (Fig. S8), SEM, TEM, HRTEM micrographs and/or EDS analysis for **ZnO$_{BD1}$-ZnO$_{BD7}$** oxides (Figs. S9-S14), N$_2$ adsorption-desorption isotherms and pore size distribution of **ZnO$_{BD1}$–ZnO$_{BD3}$** oxides (Fig. S15), UV-Vis spectra for **ZnO$_{BD1}$-ZnO$_{BD3}$** (Fig. S16) and **ZnO$_{BD4}$-ZnO$_{BD7}$** (Fig. S17) group of oxides, (Ahν)^2 vs. hν plot for determining absorption onset for **ZnO$_{BD1}$-ZnO$_{BD3}$** (Fig. S18) and **ZnO$_{BD4}$-ZnO$_{BD7}$** (Fig. S19) group of oxides, room-temperature emission PL spectra for **ZnO$_{BD4}$-ZnO$_{BD7}$** samples (Fig. S20) and for **ZnO$_{BD1}$-ZnO$_{BD7}$** oxides calcined at 500°C for 1h (Figs. S21 and S22), TEM, xHRTEM and SAED patterns of ZnO samples obtained at 140°C, for 0.25 M zinc source concentration, after 45, 90 and 180 minutes of reaction (Fig. S23), graphic representation of the level of Gram-positive (Fig. S24) and Gram-negative (Fig. S25) microbial strains growth and of the degree of microbial biofilms formed by the Gram-negative tested strains (Figs. S26-S27), the reaction pathway for the formation of ZnO oxide in BD-assisted synthesis (Scheme S1) and the SEM micrograph for ZnO product obtained in 1,2-propanediol (Fig. S28). See DOI: 10.1039/b000000x/

combination of properties, for example semiconducting, optical, piezoelectricity and pyroelectric pecularities.[1] The wide band gap (ΔE_g = 3.37 eV) and large exciton binding energy (60 meV) account for various practical applications, as ultraviolet (UV) lasers,[2] sensors,[3] solar cells,[4] (photo)catalysts[5] or cell imaging probes.[6] Recent studies highlighted the remarkable antifungal, anticancer and antibacterial activities of water-stable nano- and microsized ZnO formulations.[7]

The large variety of morphologies exhibited by ZnO, with various aspect ratios, orientations, sizes as well as crystal densities is mainly responsible for its versatile attributes.[8] The nanostructured materials combine the individual characteristics of each nanoparticle and the interactions between the adjacent crystallites generate new and interesting properties, unreachable for the corresponding 0D crystals.[1a,9] The preferential anisotropic growth along c axis of zinc oxide produces numerous one-dimensional nanostructures (1D), in which the crystallites are aligned and stacked through electrostatic interactions.[10] The two-dimensional (2D)[11] and three-dimensional (3D)[12] ZnO morphologies gave rise to new properties, different from the mono-morphologic structures. Therefore, great efforts have been devoted in the last years for developing suitable and facile synthetic methods able to tailor ZnO morphologies

toward higher dimensionalities in order to achieve new shape-induced functionalities.

The nanoparticles synthesis in organic solvents (as, for example, (poly)alcohols), represents one of the most convenient and resourceful *chimie douce* synthetic methodology for obtaining well-crystallized metal oxides with high compositional homogeneity, diversity of shapes and narrow size distributions.[13-15] The organic solvents are the main source of oxygen for the formation of metal oxides, their specific properties (polarity, viscosity, and saturated vapour pressure) influencing the nucleation process, crystal growth, particle shapes, crystallite sizes and, as a consequence, their further aggregation into higher dimension assemblies. The large number of suitable metal oxide precursors and organic solvents offers many combinations for potential reaction systems. Taking into account that both chemical (solvent, metal oxide precursor and the corresponding concentrations) and thermodynamic (temperature, pressure, etc.) factors strongly influence the size and the shape of the final nanocrystals, the rigorous choice of the organic solvent and raw material as well as the careful adjustment of the reaction conditions represent powerful tools in order to tailor the morphological characteristics of the oxide materials.[8a,14a,16]

Polyol-mediated methods turn out to be well-suited approaches for obtaining different zinc oxide morphologies, including the spherical ones.[14d,18b,19] The polyol-assisted synthesis protocol of the zinc oxide materials is simple, cost-effective, consisting in zinc salts forced hydrolysis.[14,17] The polyol peculiarities are the key parameters of the procedure: (*i*) amphiprotic nature, the polyol being able to dissolve most of the inorganic compounds; (*ii*) high boiling point (up to 250°C) that allow a wide synthesis-temperatures range; (*iii*) reducing capability, beneficial for the metal synthesis and (*iv*) a significant ability to coordinate transition metal ions. The obtained nanoparticles present an organophilic surface, derived from the polyol solvent. Such particles do not need surface modification post-treatment for further applications. However, most of the polyol approaches use inorganic/organic additives, so the risk of introducing various impurities is relatively high.

Herein we report an additive-free polyol procedure that affords, in one-step and mild conditions, highly crystalline zinc oxide nanoparticles, aggregated in hollow and solid spherical-shaped structures. We employed 1,4-butanediol (BD), which was rarely used in oxides syntheses.[20,21] The present study analyses thoroughly the mechanism of zinc oxide formation, as well as the influence of the reaction conditions (zinc source concentration and reaction time/temperature) on the final crystalline quality, morphology, surface characteristics, and thus, on the corresponding optical properties. Zinc acetylacetonate, $Zn(acac)_2$, was selected as zinc source due to its good solubility in organic solvents. Also, the high stability of *bis*-chelated $Zn(acac)_2$ determines the slow release of the zinc cations into the reaction solution and, as a result, a controlled formation of the ZnO nuclei. In order to explore the potential applications, the obtained ZnO materials were tested as photocatalysts for nitrate reduction and as antimicrobial agents, being probed against a broad spectrum of bacterial strains, both in planktonic and biofilm state.

Experimental section

The reagents of analytical grade were used without further purification.

Synthesis of ZnO nanoparticles

ZnO aggregates were obtained through a BD-assisted precipitation, as a result of the forced hydrolysis of $Zn(acac)_2$ at 90°C (samples **ZnO_{BD1}**-**ZnO_{BD3}**), 140°C (samples **ZnO_{BD4}**-**ZnO_{BD6}**) and 180°C (sample **ZnO_{BD7}**). The reaction conditions as well as the zinc precursor concentration are gathered in Table 1. In a typical synthesis, an amount of $Zn(acac)_2$ is dissolved in a known volume of 1,4-butanediol. The mixture was heated under stirring at the reaction temperature, in a round-bottom flask fitted with a reflux column, for 2-5 hours. The precipitation of ZnO occurred after 30 minutes. After cooling at room temperature, the solid phases were collected by centrifugation and washed with ethanol.

Table 1. The reaction conditions and zinc source concentrations for obtaining **ZnO_{BD1}**-**ZnO_{BD7}** oxides.

Zn^{2+} concentration (mol·l⁻¹)	Temperature/reaction time			
	90°C	140°C		180°C
	4h	2h	5h	5h
0.1	ZnO_{BD1}	ZnO_{BD4}		
0.25	ZnO_{BD2}	ZnO_{BD5}	ZnO_{BD6}	ZnO_{BD7}
0.5	ZnO_{BD3}			

Characterization of ZnO particles.

FTIR spectra (KBr pellets) were recorded with a FTIR Brucker Tensor V-37 spectrophotometer. *Thermal measurements* were performed on a Netzch STA 449 F1 Jupiter Simultaneous Thermal Analyzer apparatus in static air, with a heating rate of 10°C/min. *UV-Vis spectra* were recorded on a Perkin-Elmer Lambda-35 (200 - 1100 nm) spectrophotometer. *Photoluminescence (PL) measurements* were performed on a JASCO FP 8300 spectrophotometer using 325 nm excitation line of the xenon light. *X-ray* diffraction measurements (XRD) were carried out at room temperature on a PANalytical X'Pert PRO MPD X-ray diffractometer with Cu X-ray tube providing a Kα wavelength of 1.5418 Å. The average crystallite size (D) of the samples was determined using the Williamson− Hall equation $\beta_{hkl}\cos\theta_{hkl} = k\lambda/D + 4\varepsilon\sin\theta_{hkl}$, where λ is the wavelength of the CuKα radiation, k a constant equal to 0.9 and β_{hkl} the instrumental corrected broadening measured at the half-maximum intensity of the (hkl) peak at θ_{hkl} Bragg diffraction angle.

The size and the morphology of the particles were evaluated by *scanning electron microscopy* (SEM) and *transmission electron microscopy* (TEM). SEM measurements were carried out on field emission Hitachi H-4100FE and FEI Quanta 3D FEG microscopes. TEM experiments were

performed on a JEOL ARM 200F electron microscope operated at 200kV. *Porosity and surface area* of the samples were determined by nitrogen adsorption-desorption analysis at -196°C using a Micrometrics ASAP 2020 analyser. Specific surface areas (S_{BET}) were calculated according to the Brunauer-Emmett-Teller (BET) equation. The total pore volume (V_{total}) was estimated from the amount adsorbed at the relative pressure equal with 0.99. The average pore diameter and pore size distribution curves were obtained using Barrett–Joyner–Halenda (BJH) method from the desorption branch. *^{1}H NMR and ^{13}C NMR spectra* were recorded on a Gemini 300 BB operating at 300 MHz in DMSO-d6 using TMS as internal standard.

Photocatalytic tests. The *photocatalytic cleaning* was conducted at 18^oC in an immersion photochemical reactor made of quartz (Photochemical Reactors LTD). The reaction slurry formed from 70 mL of H_2O and 95 mg of suspended catalyst was bubbled with a mixture of 5% O_2 in Ar (30 cm^3 min^{-1}) and irradiated with a 125 W medium pressure mercury lamp characterized by a predominant radiation at 366 nm, and smaller amounts in the visible (404-579 nm) and ultraviolet (265- 334 nm) regions. The composition of the outlet gas stream was analysed every 30 minutes with a gas chromatograph equipped with TCD detectors (Buck Scientific 910). The CO_2 was separated on a Haysept column and then quantified.

The *photocatalytic nitrate reductio*n was carried out at 18 °C with 35 mg of the powder catalyst dispersed in 70 mL of an aqueous solution containing 1.61 mM (100 ppm) of NO_3^-. In order to remove the air, the reactor was purged with argon (40 cm^3 min^{-1}) while being stirred, and topped with a condenser, cooled with a recirculation chiller at -5 ^{o}C to avoid the removal by argon stream of the eventually formed NH_3. The suspended photocatalyst was irradiated with a 125 W medium pressure mercury lamp. Every 30 minutes, a sample of the solution was withdrawn from the photoreactor, filtered and the ionic species of interest (NO_3^-, NO_2^- and NH_4^+) were analysed with an ICS 900 Dionex ion chromatography system. The total ionic nitrogen concentration was evaluated according to the equation:

$$[N] = \frac{\{[NO_3^-]_0 - ([NO_3^-]_t + [NO_2^-]_t + [NH_4^+]_t)\}}{[NO_3^-]_0} * 100$$

where $[NO_3^-]_0$ represents the initial amount of nitrate (mmol) and $[NO_3^-]_t$, $[NO_2^-]_t$ and $[NH_4^+]_t$ are the amounts of the respective species (mmol) at time t (min).

Antimicrobial activity assays. The antimicrobial activity of the ZnO compounds was assayed on Gram-negative (*Escherichia coli* ATCC 13202, *E. coli* 634, *Pseudomonas aeruginosa* ATCC 27853, *P. aeruginosa* 719) and Gram-positive (*Staphylococcus aureus* ATCC 6538, *methicillin resistant S. aureus*, *Bacillus subtilis* ATCC 12488, *B. subtilis* 6833) reference (bearing the ATCC code number) and clinical bacterial strains. Microbial suspensions of 1.5 x 10^8 CFU mL^{-1} (0.5 McFarland density) obtained from 15 to 18 h bacterial cultures developed on solid media were used in our experiments. The ZnO

compound was suspended in dimethyl sulfoxide (DMSO) to prepare a stock solution of 1 mg /mL^{-1} concentration. The quantitative assay of the antimicrobial activity was performed by the liquid medium microdilution method in 96 multi-well plates. Two-fold serial dilutions of the compounds solutions (ranging between 500 μg and 0.97 μg mL^{-1}) were performed in a 200 μL volume of broth, and each was well seeded with a volume of 50 μL of microbial inoculum. Culture positive controls (wells containing culture medium seeded with the microbial inoculum) were used. The influence of the DMSO solvent was also quantified in a series of wells containing DMSO, diluted accordingly with the dilution scheme used for the complexes. The plates were incubated for 24 h at 37 ^{o}C, and the minimal inhibitory concentration (MIC) values were considered as the lowest concentration of the tested compound that inhibited the growth of the microbial overnight cultures, as compared to the positive control, revealed by a decreased value of A 600 nm.[22] For the evaluation of the influence of different concentrations on the ability of the tested bacterial strains to colonize the inert substratum, a very simple microtiter plate method was used: the microplates used for the MIC assay were emptied, washed three times by PBS (phosphate buffered saline) and the biofilm formed on the plastic wells wall was fixed for 5 min with cold methanol, coloured for 15 min by violet crystal solution and resuspended with a 33% acetic acid solution. Cell density was measured by reading the optical density of the coloured solution at 490 nm using an ELISA reader (Apollo LB 911). The minimal biofilm eradication concentration (MBEC) values were considered as the lowest concentration of the tested compound that inhibited the development of biofilm on the plate wells.

Results and discussions

The forced hydrolysis of Zn(acac)$_2$ in 1,4-butanediol affords high crystalline zinc oxide nanoparticles without any annealing post-treatment. The water amount from the zinc source (1.2 H_2O molecules for each Zn(acac)$_2$ molecule, see Figure S1 in ESI) as well as the hydroxyl groups of the organic solvent promote the hydrolysis reaction that occurs at quite low temperature (90 ^{o}C) that is, to our knowledge, one of the lowest temperature for the synthesis of zinc oxide materials carried out in polyol.[14a,f,g,18a,19c] The process is clearly accelerated with the temperature increase (140 and 180 ^{o}C), a significant amount of ZnO being obtained at these temperatures only after 2h of reaction. In order to survey the influence of reaction conditions (time, temperature, zinc source concentration) on zinc oxide particles size and shapes, several reaction parameters were analysed (see Table 1 in Experimental).

RSC Advances Accepted Manuscript

Structural, morphological, thermal and optical characterization of zinc oxide samples

FTIR spectroscopy

FTIR spectra of the zinc oxide samples for **ZnO$_{BD1}$**-**ZnO$_{BD3}$** and **ZnO$_{BD4}$**-**ZnO$_{BD7}$** series of oxides are shown in Figures S2-S4 in ESI. The spectra exhibit similar profiles, the large and very intense absorption at *ca.* 450-470 cm^{-1}, proving the presence of a zinc oxide dominant phase. The band is attributed to the phonon absorptions of the zinc oxide lattice, its energy and the absence of any splitting being specific to spherical-shaped ZnO particles.[12g,h,23] A large and multi-structured absorption covers 1600-1300 cm^{-1} range. The two medium peaks, located at 1555-1575 cm^{-1} and 1406-1412 cm^{-1}, represent the signature of $\nu_{(C=O)}$ stretching vibrations of the acetylacetonate molecules. These bands associated with the large absorption centred at 3400 cm^{-1}, specific to the hydroxyl groups, suggest the formation of the basic layered zinc hydroxide compound either as intermediate product (see below, the XRD analysis). The adsorption of acetylacetonate molecules on zinc oxide polar surfaces is not excluded. The ^{1}H NMR and ^{13}C NMR spectra recorded on the supernatant solution of **ZnO$_{BD2}$** and **ZnO$_{BD7}$** samples confirm the presence of small quantities of acetylacetonate molecules (see Figures S5 and S6 in ESI).

For all materials, the presence of a medium intensity splitted band, with peaks at 1049 and 1020 cm^{-1}, indicates traces of diols, most likely attached to the polar ZnO surfaces, through hydrogen bonds. A high-energy band, centred at ca. 3400 cm^{-1} attributed to ν(O-H) stretching vibration originating from water, diol and/or layered zinc acetylacetonate hydroxide molecules is observed for all products.

Thermal analysis

The thermal behaviour of the synthesized samples is similar (Figure S7 in ESI). The total mass loss lies between 3 and 5%, of which about 1.5-2 % is water that is evolved gradually up to 170 ^{o}C. Commonly, the organic components (entrapped solvent and reaction by-products) are eliminated in three steps: about two-thirds of the organic mass loss is removed *via* two distinctive exothermic processes that occur up to ~ 450 ^{o}C, while the remaining third were slowly decomposed through a continuous mass loss stage that takes place up to 1000 ^{o}C.

XRD analysis

The XRD diffractograms of **ZnO$_{BD1}$**–**ZnO$_{BD3}$** oxides are presented in Figure 1 and those corresponding to **ZnO$_{BD4}$**–**ZnO$_{BD7}$** in Figure S8 in ESI. The lattice parameters and the crystallites sizes values of the ZnO phase are gathered in Table 2. ZnO würtzite-type phase (JCPDS no. 36-1451) is formed in all cases, but its purity and crystallite sizes depend on the synthesis conditions. A layered basic double hydroxide zinc

phase (LDH-Zn), identified as impurity, is present in low-temperature samples, with a high zinc concentration (traces in **ZnO$_{BD2}$** and relatively well-defined in **ZnO$_{BD3}$**). The formation of the LDH-Zn in polyol-assisted reaction (diethylene glycol and ethylene glycol) is not unusual.[24] In our case, LDH-Zn is most likely an intermediate product, that, in specific conditions, is converted into zinc oxide.
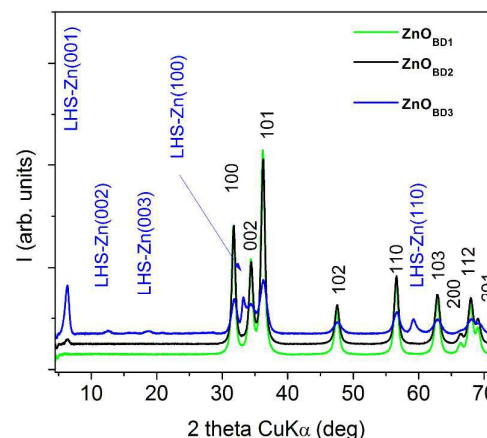

Figure 1. The XRD difractograms recorded for **ZnO$_{BD1}$**-**ZnO$_{BD3}$** samples.

The samples, in which LDH-Zn was detected, were obtained in the most unfavourable conditions for its conversion to ZnO (low temperature, short reaction time, high concentration of zinc). In other words, the absence of LDH-Zn does not mean that, in these cases, the formation of ZnO did not occur *via* LDH-Zn intermediate. For **ZnO$_{BD3}$**, the reflections of the layered hydroxide zinc phase could be clearly identified, the lattice parameters (*a* = 0.312 nm and *c* = 0.141 nm) being quite close to the Zn(OH)$_{1.58}$(CH$_3$COO)$_{0.42}$·0.31H$_2$O standard (JCPDS no. 56-0569, with *a* = 0.3138 nm and *c* = 0.1475 nm, respectively).[24] For **ZnO$_{BD2}$** only the (001) peak of the layered basic zinc hydroxide (*c* = 0.139 nm) could be discerned.

Table 2. Structural and morphological data of the ZnO samples.

Sample	Crystalographic data			D (nm)	BET surface area (m²/g)	V_{total} (cm³/g)*	ZnO aggregates morphologies and dimensions
	a (nm)	*c* (nm)	*c/a*				
JCPDS no. 36-1451	0.324982	0.520661	1.602	-	-	-	-
ZnO$_{BD1}$	0.3254	0.5206	1.600	13.2	91.9	0.334	hollow spheres, ~250 nm
ZnO$_{BD2}$	0.3209	0.5209	1.602	13.1	34.9	0.215	solid porous spheres, ~100 nm
ZnO$_{BD3}$	0.3247	0.5212	1.605	8.1	43.2	0.152	particle agglomeration, rarely spheres up to ~50 nm
ZnO$_{BD4}$	0.3257	0.5214	1.601	9.9	-	-	solid spheres, 170-200 nm
ZnO$_{BD5}$	0.3254	0.5211	1.601	10.4	31.7	0.370	solid spheres, ~ 50 nm
ZnO$_{BD6}$	0.3251	0.5208	1.602	11.6	40.3	0.346	particle agglomeration, rarely spheres; up to ~50 nm
ZnO$_{BD7}$	0.3250	0.5210	1.603	9.9	32.1	0.249	solid spheres, ~100 nm

*V_{total} = total pore volum

As far as the crystallite sizes are concerned, the low-temperature samples (**ZnO$_{BD1}$** and **ZnO$_{BD2}$**) have the highest dimensions (~ 13 nm). The particle sizes decreased with the increasing zinc concentration (8.1 nm for **ZnO$_{BD3}$**) and reaction temperature (11.6 and 9.9 nm for **ZnO$_{BD5}$**, respectively **ZnO$_{BD7}$** samples) due to the higher number of the formed nuclei in solution.[25] The reaction performed at the highest temperature (180 °C) generated the smallest crystallites (**ZnO$_{BD7}$**). Crystallite sizes did not change dramatically with reaction time, compared with temperature, suggesting that the reaction time has less effect on the growth rate of the primary, nanosized crystals. Nevertheless, the reaction time/temperature parameters influence the agglomeration of primary crystals to produce secondary structures (investigated by electron microscopy).

SEM and TEM analysis

The morphology of the ZnO materials depends on the zinc salt concentration and the reaction conditions (*vide infra*). A significant effect of the zinc source concentration on the ZnO morphology is observed for the low-temperature ZnO samples (90 °C, **ZnO$_{BD1}$**-**ZnO$_{BD3}$**). Uniform hollow spheres of *ca*. 250 nm in diameter (see Figure 2 and Figure S9 in ESI) are obtained using a zinc concentration equal to 0.1 M (**ZnO$_{BD1}$**). The spherical shell is assembled from several layers of ZnO crystallites forming a hollow cavity of *ca*. 100 nm. This is a very rare example of ZnO spherical aggregates with hollow cores, obtained through a polyol-mediated method.[19i,j] For richer-zinc experiments **ZnO$_{BD2}$** (0.25 M), solid spheres are formed, with noticeable lower diameters (*ca*. 100 nm, see Figure 3 and Figure S10 in ESI). The aggregates are constituted of many small crystallites and irregular nanopores of several nanometers.
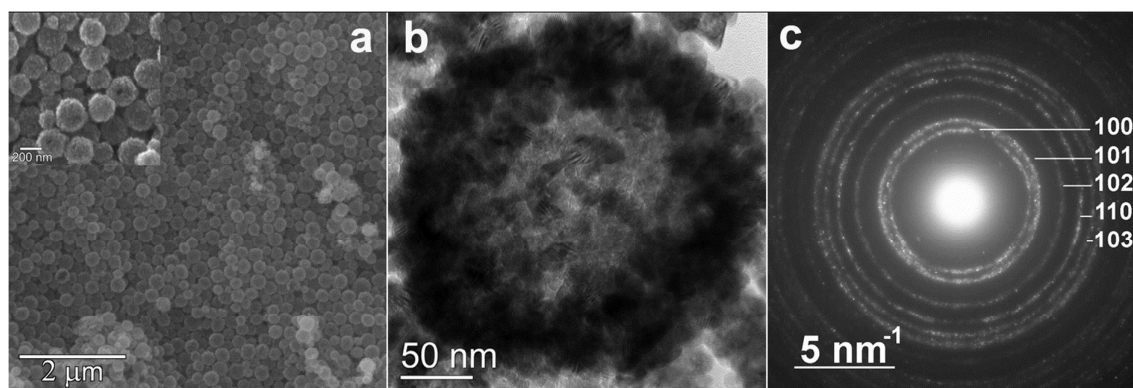

Figure 2. (a) SEM panoramic micrograph (inset: magnified SEM image); (b) TEM image of a single-sphere showing the hollow internal structure for **ZnO$_{BD1}$** sample and (c) SAED pattern corresponding to TEM image.
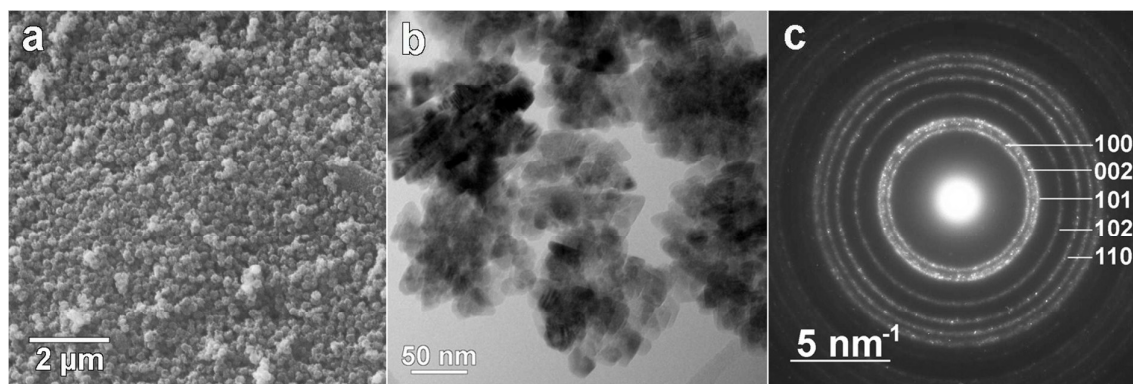
Figure 3. (a) SEM panoramic micrograph; (b) TEM micrograph and (c) the corresponding SAED pattern for **ZnO_BD2** sample.

At the highest concentration of zinc precursor **ZnO_BD3** (0.5 M), the agglomeration of the particles does not occur in a well-defined pattern, small particles coexisting with seldom, small spherical structures (with a diameter up to *ca.* 50 nm, see Figure S11 in ESI).

The reaction performed at increased temperature (140 ^{o}C), for 2h, and using 0.1M zinc concentration (**ZnO_BD4**), gave rise to well-formed solid spheres (170-200 nm in diameter), built from 3D-connected nanocrystals, most of them showing distorted spherical shapes (Figure 4). TEM images indicate that the spheres exhibit an external porosity (Figure 4b).

In the same reaction conditions (140 ^{o}C, 2h) the increase of zinc precursor concentration up to 0.25M (**ZnO_BD5**, see Figure S12 in ESI) determines also the aggregation of ZnO crystallites into solid structures, relatively well-delimited, but with lower diameters (*ca.* 50 nm) than those corresponding to **ZnO_BD4** oxide. By keeping constant the Zn(acac)$_2$ concentration (0.25 M), we further survey the influence of the reaction parameters: time and temperature. A longer reaction time (5h) affects the integrity of the polycrystalline aggregates, as in the case of **ZnO_BD6** product: agglomerates of spherical particles, with sizes lower than 50 nm that coexist with dispersed particles (Figure 5 and Figure S13 in ESI). A higher reaction temperature (180 ^{o}C) is beneficial for the formation of uniform, well-defined solid spherical morphologies (**ZnO_BD7**) of ~100 nm, assembled from small zinc oxide crystallites closely compacted. No isolated nanocrystals were found (Figure 6 and Figure S14 in ESI).
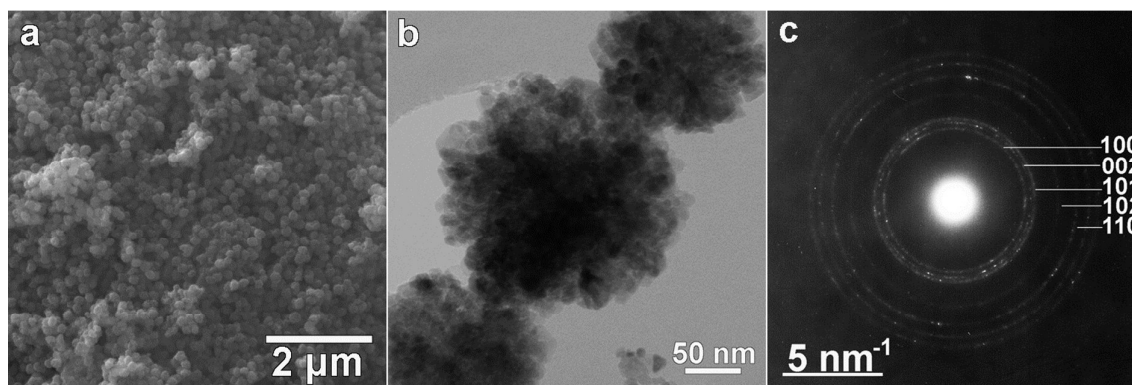

Figure 4. (a) SEM panoramic micrograph, (b) TEM micrograph at higher magnification and (c) corresponding SAED pattern for **ZnO_BD4** sample.
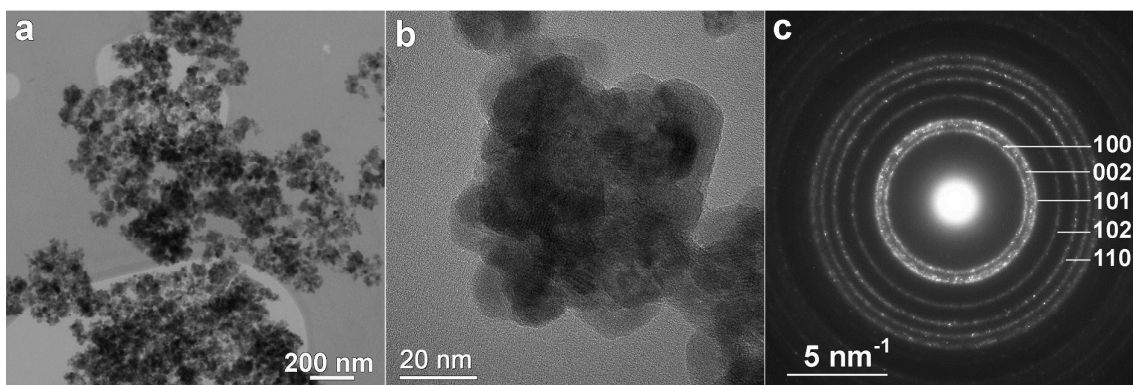
Figure 5. TEM micrographs (a) panoramic image, (b) high-magnification image and (c) corresponding SAED pattern for **ZnO_BD6** sample.
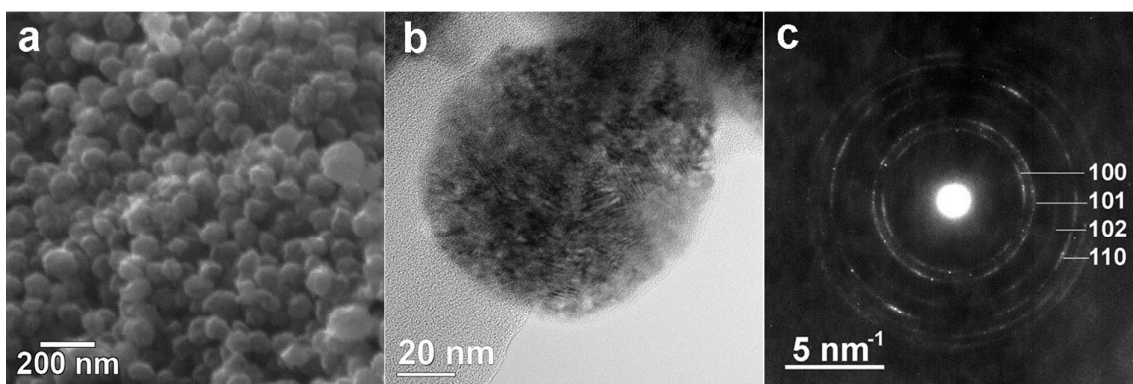

Figure 6. (a) SEM panoramic micrograph, (b) high-magnification TEM micrograph image and (c) the corresponding SAED pattern for **ZnO_BD7** sample.

BET analysis

All the adsorption desorption isotherms are of type IV, accompanied by a H3 type hysteresis loop, according to IUPAC classification (Figure S15, top in ESI). Usually this type of isotherm is attributed to predominantly mesoporous samples, with interconnected pore systems. The highest surface area (91.9 m^2/g) and total pore volume (0.334 cm^3/g) was measured for poor-zinc and low-temperature sample, **ZnO_BD1** (0.1M/90°C). The pore size distribution (PSD) for **ZnO_BD1** oxide is trimodal, with peaks centred at about 5, 16 and 30 nm (Figure S15 bottom in ESI). This is in good agreement with the microscopy investigations that reveals highly porous spherical aggregates in which the irregular pores are randomly distributed. The zinc oxide samples obtained using higher concentrations of Zn(acac)$_2$ precursor, **ZnO_BD2** and **ZnO_BD3**, have relatively close S$_{BET}$ values, but the total pore volume is lower at the highest concentration (0.5M). The PSD curves for these two samples show broad distribution of mesopores with two peaks centred at 7 and 29 nm for **ZnO_BD2** and one wide peak at ~16 nm for **ZnO_BD3**. The sharp peak at ~ 3.5 nm present on both curves appears as a result of the tensile strength effect (TSE) and can be considered an artefact (Figure S15

bottom in ESI).[26] The TSE effect occurs when the interconnected pores filled with nitrogen are suddenly emptied through narrower pores, being accompanied by a forced closure of the hysteresis loop at relative pressure values between 0.4 and 0.45.

Longer reaction time and higher reaction temperature increase the grade of particle agglomeration which results in an increased average of the pores diameter of the samples (see Table 2, samples **ZnO_BD5**-**ZnO_BD7**). The N$_2$ sorption isotherms for these samples have similar profiles as above discussed **ZnO_BD1** - **ZnO_BD3** samples (see Figure 7a). The nitrogen uptake does not reach a plateau indicating the existence of relatively large mesopores, with wide pore size distributions. The pore volume *vs.* pore diameter curves (Figure 7b) of **ZnO_BD5** and **ZnO_BD6** samples show peaks centred at 31 and 23 nm respectively, whereas **ZnO_BD7** exhibits bimodal distribution with peaks maxima at around 9 and 48 nm. The variation of both BET surface area and pore volume could be correlated with the formation of aggregates of ZnO nanoparticles of various dimensions.

To our knowledge, **ZnO_BD1** sample exhibits the highest mesoporous area for ZnO obtained following a polyol-based procedure. ZnO with a microporous area of 80 m^2/g was obtained in diethyleneglycol (DEG),[14a] mesoporous and

macroporous sheets of zinc oxide with a surface of 25.74 m^2/g were reached using ethyleneglycol,[18c] while, a reaction carried on in DEG afforded mesoporous ZnO nanoclusters with a surface area equal to 20.6 m^2/g.[27]
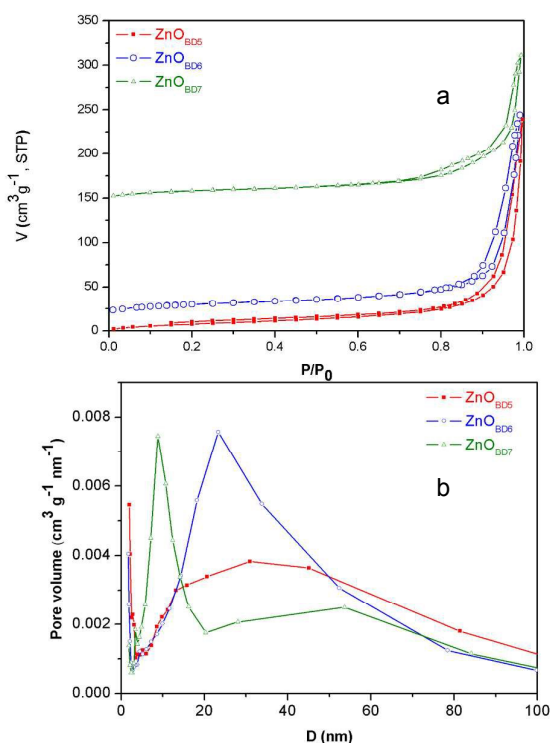

Figure 7. (a) N_2 adsorption–desorption isotherms of **ZnO$_{BD5}$–ZnO$_{BD7}$** samples (for clarity the curves were shifted up by: 20 units for **ZnO$_{BD6}$**, 150 units for **ZnO$_{BD7}$**); (b) Pore size distribution of **ZnO$_{BD5}$–ZnO$_{BD7}$** samples.

Optical properties

UV-Vis spectroscopy

The absorption spectra of **ZnO$_{BD1}$-ZnO$_{BD3}$** oxides are presented in Figure S16, while for **ZnO$_{BD4}$-ZnO$_{BD7}$** in Figure S17 in ESI. All zinc oxide samples show very similar profiles, a strong and large absorption band covering the UV region. Two distinctive shoulders are distinguished: the lower energy peak (350 nm) is most likely a result of the electronic transition from the valence band to the conducting band ($O_{2p} \rightarrow Zn_{3d}$),[28] whereas the second one, located at 250 nm, is associated with defects that usually alter the würtzite-type ZnO structure.[29] The band gap energy (*Eg*) of the zinc oxide aggregates can be determined by the extrapolation of the linear part of the absorption coefficient *vs* exciting energy (hν) curves to zero.[30] In our case, the estimated values range between 3.12 and 3.3 eV (Figures S18 and S19 in ESI).[31]

Photoluminescence spectroscopy (PL)

A defect analysis of the zinc oxide samples was carried out through the investigation of their photoluminescence (PL) properties. Room-temperature PL spectra of the **ZnO$_{BD1}$-ZnO$_{BD3}$** are presented in Figure 8 and of **ZnO$_{BD4}$-ZnO$_{BD7}$**, in Figure S20 in ESI.

Generally, ZnO exhibits a sharp and highly intense emission in the near UV (near band-edge emission) generated by the free-exciton recombination[31] and some visible bands (known as deep level emissions), caused by structural defects and impurities.[32]
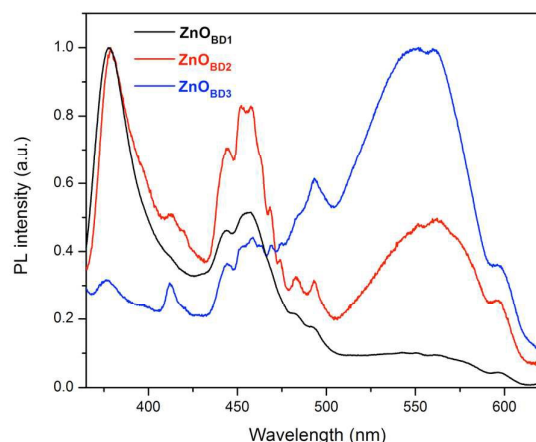

Figure 8. Room-temperature emission PL spectra for **ZnO$_{BD1}$-ZnO$_{BD3}$** samples.

The PL spectra for both **ZnO$_{BD1}$-ZnO$_{BD3}$** and **ZnO$_{BD4}$-ZnO$_{BD7}$** groups of oxides show UV emissions, the majority of them being strong in intensity and located at *ca*. 375-380 nm. Two "extreme" samples, rich-zinc **ZnO$_{BD3}$** and high-temperature **ZnO$_{BD7}$** oxides show weak UV peaks. The different intensity of the band gap bands for **ZnO$_{BD3}$** and **ZnO$_{BD7}$** oxides is caused by several factors that, most likely, act simultaneously: different concentration of the specific defects, different aggregated morphologies and/or the presence of impurities.[34] In the visible region, all zinc oxide samples present multi-structured violet-blue (410-480 nm) emissions and a broad green emission (*ca*. 550-560 nm). The attribution of these emissions is often controversial and strongly depends on the material peculiarities. For our samples, the most interesting aspect of the visible zone is the presence of violet-blue emission bands, which are rarely detected in the PL spectra of zinc oxide. The violet-blue bands could result from zinc vacancies, interstitial zinc defects[35] and/or are associated with the presence of chemical species attached on the ZnO surface.[14e,36] The broad green emissions are generally related with the oxygen deficiency defects and appear especially in the case of high-surface area zinc oxide materials.[33a,37] According to this hypothesis, the weak green emission for **ZnO$_{BD1}$** oxide, characterized by the highest surface area (91.9 m^2/g), is somewhat surprising. Weak green emissions are observed also for **ZnO$_{BD4}$** (0.1M/140 ^{o}C) and **ZnO$_{BD5}$** (0.25M/140 ^{o}C) samples

suggesting that, in these cases, the amount of zinc cations does not significantly influence the oxygen-related defects. The strongest green emissions found for ZnO$_{BD3}$ (0.5M/90 ^{o}C) and ZnO$_{BD7}$ (0.25M/180 ^{o}C) oxides associated with their corresponding weak UV peaks, indicate a significant concentration of the oxygen-related defects (both intrinsic and extrinsic). For all zinc oxide samples are observed weak yellow shoulders, blue-shifted to 590 nm, emission usually attributed to the presence of interstitial oxygen defects.[32a,33a,38] In this stage of research, such complexity of the visible emission patterns of zinc oxide materials could not provide us accurate information about the defect types in our samples, nor the influence of the reaction parameters. It is very likely that the extrinsic factors (surface defects, size of the crystalline aggregates) strongly influences the energy and intensity of the visible emissions, competing with the deep level defects and giving rise to "atypical" curve profiles. In an attempt to clarify the origin of the visible emissions, room temperature PL spectra were performed on ZnO materials, calcined at 500°C for 1h (Figures S21 and S22 in ESI). The PL spectra show both UV and visible (blue-violet and green-yellow) emissions, but with different intensities compared to the non-calcined samples. This indicates a rearrangement of the shallow and deep oxygen and zinc-related defects. The very intense blue-violet emission correlated with quasi-supressed green emissions and less intense UV band could be determined by the removing of the surface-attached organic residua, through thermal treatment, but also could be a result of the structural changes (particles/aggregates sizes, defect types and concentrations) during the calcination process. However, the predominance of the blue-violet emission for the calcined samples opens very interesting perspectives for biological fluorescence labelling applications.[35a]

Mechanism of zinc oxide formation

Scheme S1 summarizes a possible reaction path for the formation of zinc oxide through the hydrolysis reaction of zinc acetylacetonate in 1,4-butanediol (BD). 1,4-butanediol acts as reactant and exclusive solvent. The nucleophilic attack of the hydroxyl groups of polyols on the carbonyl bonds of the acac ligand, associated with a hydrolysis reaction gives rise to Zn-OH species, with the esterification of BD and release of acetone. The ester is identified as by-product in the ^{1}H NMR and ^{13}C NMR spectra performed on the supernatant solutions of ZnO$_{BD1}$ and ZnO$_{BD2}$ (see Figures S4 and S5 in ESI). An important step of the reaction is the formation of LDH-Zn intermediate that is further dehydrated and assembles the Zn-O-Zn-O- sequences. It is very likely that the formation of LDH-Zn intermediates takes place for all zinc oxide samples, independently of the reaction parameters. As shown above, their conversion into zinc oxide is not completed for the low-temperature and high zinc concentration samples, ZnO$_{BD2}$ and ZnO$_{BD3}$ as they were identified as impurities by XRD analysis.

The growth of the ZnO nanostructures follows a two-stage mechanism: the nucleation of small primary ZnO particles in supersaturated solution and further, their aggregation through an oriented attachment mechanism, into spherical-shaped structures. Freshly formed nanocrystals, capped with organic molecules (hydroxyl-based products) have a strong tendency to aggregate into low-energy spherical structures that decrease the surface energy of the nanoparticles. The BD viscosity associated with its high boiling point determines a kinetically slow nucleation rate and a migration of ZnO crystallites that will allow time for the particles to gather into stable spherical structures. The adjustment of the reaction parameters modulates the aggregates sizes and morphologies (see Scheme 1).

The zinc cations concentration strongly influences the internal structure and cohesion degree of the polycrystalline microspheres. In the same reaction conditions (90 ^{o}C/4h), a step-wise increase of Zn(acac)$_2$ amount, from 0.1M to 0.5M, determines an evolution from well-defined hollow (0.1M) and solid (0.25M) microspheres toward less-coherent agglomerates (0.5M). The sizes of the ZnO clusters also diminish with the increase of the zinc content (from 250 to ca. 50 nm).
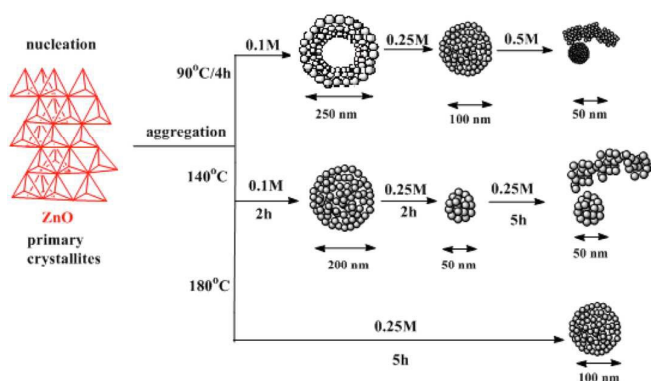
Scheme 1. The development of different spherical ZnO morphologies.

Most probably, a higher concentration of the zinc precursor accelerates the hydrolysis reaction, which generates an increased number of nuclei that will further form smaller ZnO aggregates. By keeping constant the Zn precursor concentration, raising the reaction temperature up to 140 ^{o}C for a shorter reaction time (2h), we obtained smaller solid ZnO nanoclusters, most likely due to a similar acceleration of the hydrolysis/dehydration processes. A longer reaction time (5h), at constant temperature and zinc content (140°C/0.25M) produces undefined agglomerates of ZnO clusters (up to ca. 50 nm). A further increase of the temperature (180 ^{o}C/5h/0.25M), yielded larger, well-defined ZnO spheres (up to 100 nm).

A time-dependent experiment was carried out in order to survey the evolution of the morphology of ZnO materials. The samples were obtained at 140°C for 0.25M zinc cations concentration, after 45, 90 and 180 minutes. Figure S23 in ESI shows the TEM micrographs (at low and high magnification) and SAED patterns for the above-mentioned samples. It is observed that, after 45 minutes of reaction, the quasi-

spherical particles are aggregated in less-compact spherical assemblies that are interconnected into a necklace-like arrangement, showing external and internal porosity. The size of the ZnO aggregates increases with the reaction time, from *ca*. 50-60 nm (after 45-120 minute) up to *ca*. 100 nm (after 180 minutes of reaction). The longer reaction time, more compact and more defined ZnO particles spherical assemblies are formed.

The formation of the spherical-shaped aggregates with hollow structure is very unusual in polyol-assisted reaction. For example, mesoporous and hollow ZnO microspheres were obtained in PEG-assisted one-step reaction.[19j] It is very likely that the void formation for **ZnO$_{BD1}$** is similar and could be related with the different crystallization degree between the ZnO surface crystallites and the inner ones, caused probably by the low concentration and non-uniform distribution of the zinc cations. In the early stage of reaction, the particles are agglomerated into larger clusters. At the surface, the particles are well-crystallized and further grow larger, through an Oswald ripening process, while the weakly crystallized ZnO particles from the core of the microspheres are dissolved, forming, in the initial stages, internal pores that, as the reaction progresses, merge and finally hollowing the structure. This could explain the largest particle sizes (13 nm) and BET surface area obtained for **ZnO$_{BD1}$** sample. The low temperature (90 °C) is probably the key parameter that determines the distinct morphology evolution. Further investigations are currently dedicated to the elaboration of a general polyol-assisted method to obtain metal oxides with tuned sizes/morphologies, in mild conditions.

Photocatalytic activity

Photocatalytical experiments were carried on **ZnO$_{BD7}$** sample (0.25M/180 °C). The photocatalytical experiments are related to the presence of the organic coatings on the ZnO surface and were performed in order to: (*i*) use the light irradiation as an alternative possibility for surface cleaning and (*ii*) exploit the organic moieties as hole scavengers in photocatalytical reduction reaction of NO$_3^-$.

The first case arises from the requirement of a "clean" ZnO surface in some particular applications. The photocatalytical processes may be used as an elegant, non-destructive, low-temperature surface-cleaning alternative (18 °C), avoiding hence the nanoparticles agglomeration that occurs during high temperature elimination of the organic compounds. The photo-mineralization of the coated organic compounds is accompanied by CO$_2$ formation, of which release has a linear dependence with reaction time (Figure 9). The slower increase of CO$_2$ amount in the first 200 min of irradiation can be explained by its partial dissolution in water associated with carbonic acid development. Once the solution is saturated with CO$_2$, the rate of formation is stabilized at a higher value. In accordance with literature data, the photo-mineralization of organic compounds obeys a zero order kinetic law:[39] the experimentally determined apparent rate constant of 1,4-

butanediol degradation normalized by catalyst weight in steady state regime being 0.6 mmol CO$_2 \cdot h^{-1} \cdot g_{cat}^{-1}$. The photonic efficiency (ξ), defined as the number of molecules of CO$_2$ formed in one second divided by the number of incident photons (for our photoreactor and lamp configuration, $\phi = 7 \times 10^{18}$ photons$\cdot s^{-1}$) is 0.014%.

Being known that groundwater contamination with nitrate (originating from agricultural activities and urban development) represents a serious risk to human health,[40] the capacity of the capped ZnO materials to reduce photocatalytically the contaminant to gaseous nitrogen compounds was also investigated. The general consensus is that the photocatalytic reduction of NO$_3^-$ occurs only over semiconductor photocatalysts (mainly TiO$_2$) modified with one or more metals mostly noble ones (such as Ru,[41a] Ag,[41b,c] Ni,[41d,e] Ni-Cu,[41f,g] Pt-Cu,[41h,i] Pd-Cu,[41g,i,j] and Sn-Pd[41k]), in the presence of organic additives that act as hole scavengers (alcohols, small molecule organic acids, humic acids *etc*.).[42] So far, ZnO has been considered photocatalytically inactive for the reduction of NO$_3^-$ and, to date, no data were reported on this subject. The idea underlying the performed photocatalytic tests is to take advantage of the organic compounds (derived from acetylacetonate and polyol) adsorbed on the ZnO surface, and to use them as hole scavenger in the photocatalytic denitration process.
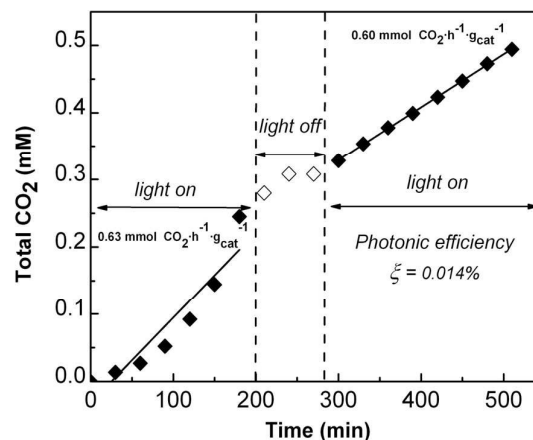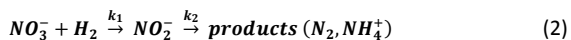

Figure 9. Time course of CO$_2$ formation through photoirradiation of **ZnO$_{BD7}$** sample.

The evolution of species involved in denitration process can be modelled by considering the following successive first order reactions (equation 2) with the corresponding k_1 and k_2 apparent reaction rate constants (equations 3, 4):
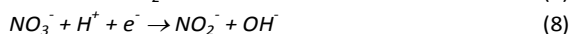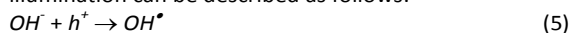
$$NO_3^- + H_2 \overset{k_1}{\to} NO_2^- \overset{k_2}{\to} products\ (N_2, NH_4^+) \qquad (2)$$

$$\frac{dC(NO_3^-)}{dt} = k_1 C(NO_3^-) \qquad (3)$$

$$\frac{dC(NO_2^-)}{dt} = k_1 C(NO_3^-) - k_2 C(NO_2^-) \qquad (4)$$

The composition-time profiles from Figure 10A show that (*i*) NO_3^- concentration decreases sharply to zero within the first 90 min of irradiation; (*ii*) the NO_2^- amount increases to a maximum of 1.48 mM (68.36 ppm) in the first 30 min and then decreases slowly, reaching at the end of reaction time (240 min) a level of 0.35 mM (16.13 ppm). The formation of ammonia is negligible: at 240 min the concentration of NH_4^+ is 0.018 mM (0.32 ppm) meaning that the photocatalyst shows a high selectivity toward N_2 under light irradiation conditions. The decrease in total ionic nitrogen at the end of test was 77.6 %. The best fit of the experimental data (NO_3^-, NO_2^- concentration *vs*. time) is obtained for k_1 and k_2 equal with 0.085 and 0.0075 min^{-1} respectively.

At the surface, the degradation of organic compounds occurs either through an indirect or direct oxidation by photo-produced holes.[43] While in the indirect mechanism, the organic compounds are degraded *via* OH· radicals formed by earlier oxidation of water at the surface by the positive holes (eq. 5), in the direct oxidation mechanism, the photogenerated holes react directly with the organic substrate to form $CO_2^{\bullet -}$ radical species ($E^0(CO_2/CO_2^-)$ = -1.8 eV) and finally CO_2 (eqns. 6 and 7).[41c,44] The NO_3^- species are reduced by photogenerated electrons to NO_2^- intermediate and finally to N_2 and NH_4^+ (see eqns. 8 and 9).[45]

The oxidation and reduction processes taking place under illumination can be described as follows:

$$OH^- + h^+ \to OH^{\bullet} \qquad (5)$$

$$R\text{-}H + OH^{\bullet} \to CO_2 \qquad (6)$$

$$R\text{-}H + h^+ \to CO_2^{\bullet -} \qquad (7)$$

$$NO_3^- + H^+ + e^- \to NO_2^- + OH^- \qquad (8)$$

$$NO_2^- + H^+ + e^- \to N_2, NH_4^+, OH^- \qquad (9)$$

In order to prove the polyalcohol role as hole scavengers in photodenitration process, the reaction was repeated on the ZnO sample previously cleaned by photoirradiation (Figure 10B). It can be observed that the photocatalyst deactivates rapidly, within the first 60 min of irradiation time. The concentration of NO_3^- decreases to 0.17 mM (10 ppm NO_3^-), remaining afterward unchanged. The concentration of NO_2^- reached a maximum of 1.16 mM (72 ppm) at 90 min, decreasing then slowly in time to 1 mM (66 ppm NO_2^-). Over the photo-cleaned ZnO sample a diminution of only 21.8 % in total ionic nitrogen was registered. Because of the catalyst deactivation, the rate constants were calculated only for the first three experimental points.
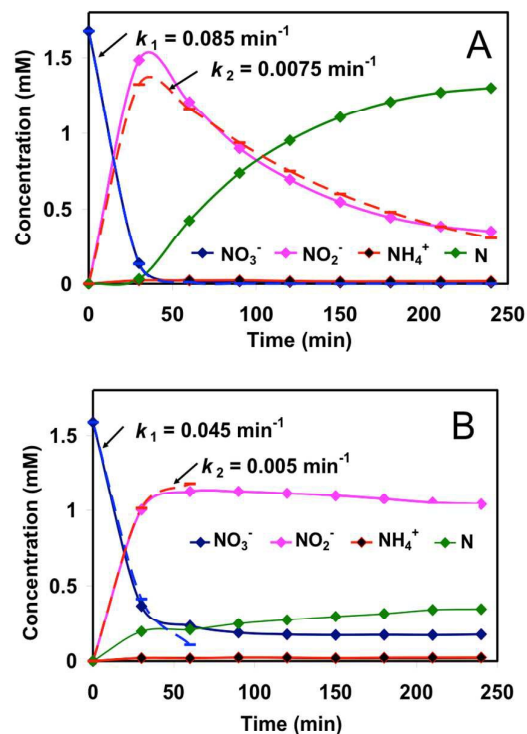

Figure 10. Time course of reactant (NO_3^-) and products (NO_2^-, NH_4^+, N (N_2)) during denitration over organic-capped ZnO nanoparticles (as prepared) (A) and over ZnO cleaned by light irradiation (B).

Based on the experimental results, it is clear that photoreduction processes of NO_3^- and NO_2^- takes place only in the presence of the organic hole scavenger (*i.e.* BD). Once the organic substrate is completely mineralized, the denitration activity becomes negligible.

Antimicrobial activity

Recent advances in the field of material science, particularly the ability to prepare well defined nanostructures with diverse morphologies, have led to the development of new inorganic biocidal agents.[46] ZnO has a large spectrum of antibacterial and antifungal properties being active against Gram-negative and Gram-positive bacteria, halophilic bacteria, yeasts, molds, even against high-temperature and high-pressure resistant endospores.[47] Moreover, ZnO proved to be a promising material for anti-parasitical applications, proving acaricidal, pediculocidal and larvicidal activity.[48] ZnO also has excellent stability, biocompatibility and longer shelf life compared to organic antimicrobial agents.[49] Despite the increased incidence of the infections produced by multiresistant pathogenic bacterial strains derived from biofilms developed on host tissues and on implanted biomaterials, to date, the anti-biofilm activity of inorganic agents has scarcely been investigated.[53]

In this context, both the antimicrobial and anti-biofilm activity against Gram-positive and Gram-negative reference and clinical strains were investigated, the tests being performed for the **ZnO$_{BD6}$** oxide (140 ^{o}C, 5h, 0.25M).

The antimicrobial activity against the two *Pseudomonas aeruginosa* strains grown in planktonic form is particularly high, the minimal inhibitory concentration value (MIC) of 62.5 µg mL^{-1} being much lower than those previously reported.[49] Although the *E. coli* strains proved to be the least susceptible to the tested compound, however, the obtained MIC values ranging from 250 to 500 µg mL^{-1} are smaller or at least equal with those reported in other studies.[50d,51] The tested compound inhibited drastically the growth of Gram-positive strains at MICs of 125-250 µg mL^{-1} (Table 3 and Figures S24-S27 in ESI), which are lower than those reported in other similar studies.[52] Surprisingly, in case of *S. aureus* and *B. subtilis* strains, the clinical strains were more sensitive than the ATCC reference strains, as revealed by the lower MIC values (125 µg mL^{-1} *versus* 250 µg mL^{-1}, Table 3).

The **ZnO$_{BD6}$** sample, at high concentrations, inhibited the ability of both Gram-positive and Gram-negative strains to form biofilms, the MBEC value being of 500 µg mL^{-1} for the majority of the tested strains, excepting *B. subtilis* ATCC 12488 (62.5 µg mL^{-1}) and *P. aeruginosa* ATCC 2785 (31.25 µg mL^{-1}) (Table 3). The good anti-biofilm activity against *P. aeruginosa* is remarkable, considering that this pathogen is one of the most powerful agent of biofilm associated infections, particularly in cystic fibrosis patients, in which it can cause particularly devastating chronic lung infections or facilitate the occurrence of life-threatening nosocomial infections in short time courses.[54] Furthermore, biofilm cells of *P. aeruginosa* are much more resistant to semiconductor stress than their planktonic counter-parts.[50c]

Table 3. MIC and MBEC values (µg mL^{-1}) of the tested compounds on the Gram-positive and Gram-negative reference and clinical strains in planktonic and biofilm form.

Gram-positive strains	MIC	MBEC	Gram-negative strains	MIC	MBEC
S. aureus ATCC 6538	250	500	*P. aeruginosa* ATCC 27853	62.5	31.25
MRSA	125	500	*P. aeruginosa* 719	62.5	500
B. subtilis ATCC 12488	250	62.5	*E. coli* ATCC 13202	250	500
B. subtilis 6683	125	500	*E. coli* 634	500	500

Conclusions

Hollow and solid zinc oxide spheres (with diameters from 50 to 250 nm), of high crystalline quality, were obtained following a facile additive-free polyol approach, through the forced hydrolysis of the zinc acetylacetonate in 1,4-butanediol. The adjustment of the synthesis parameters (reaction time and temperature, zinc cation concentration) tunes the size of ZnO crystallites, the size and the shape of the ZnO aggregates, as well as the surface characteristics and nature/concentration of the defects and, as a consequence, the luminescent properties. The lowest reaction temperature and Zn^{2+} concentration (90 ^{o}C, 0.1 M) afforded ZnO homogenous microspheres assembled from layers of ZnO nanocrystallites, with hollow cores. This is a quite rare morphology type for the zinc oxide products obtained following a polyol-based procedure. The increase of the reaction temperature and time and the higher amounts of zinc cations determine an evolution of the internal structures of the micro-aggregates, from hollow to solid and well-defined spheres toward a less-coherent arrangement of the morphologies. BD plays a crucial role in the assembly of coherent spherical aggregates, this aspect being best evidenced by comparing the morphologies of the ZnO products obtained, in the same reaction conditions, in 1,2-propanediol and BD (see Fig. S28 in ESI). The reaction mechanism, supported by ^{1}H NMR, ^{13}C NMR and XRD analyses, indicates an initial nucleophilic attack of the polyol hydroxyl groups on the acac ligand, followed by a hydrolysis reaction with the formation of zinc layered double hydroxide intermediate, which further is transformed to ZnO. A time-dependent experiment proved that ZnO spherical aggregates are formed in the early stages of the reaction (45 minutes), the assemblies becoming larger, more compact and coherent after a longer reaction time (180 minutes).

The spherical-shaped ZnO materials exhibit high surface areas (up to ~ 92 m^2/g) and mesopores, being of interest for (photo)catalytical reactions. The exploration of the photocatalytic activity, under visible irradiation, gave remarkable results in the denitration reaction in terms of nitrate conversion and N$_2$ selectivity, highlighting the importance of the capping organic species. This opens new perspectives in developing performant "two in one" formula photocatalysts, namely a wide-band semiconductor with an organic coating that works as hole scavenger. ZnO spherical morphologies proved to have good antimicrobial and anti-biofilm activities, suggesting their potential for the development of novel antimicrobial formulations.

The BD-assisted method represents a viable route to build ZnO spheres with hydrophilic properties of which potential applications are far from being fully explored. These results are very encouraging and further studies are currently carried on in order to expand the BD-mediated approach for the controlled synthesis of other types of nanostructured, simple or binary, metal oxides.

Acknowledgements

ARTICLE

Notes and references

1   (a) M. Ahmad, J. Zhu, *J. Mater. Chem.*, 2011, **21**, 599; (b) A. B. Djurišić, X. Chen, Y. H. Leung**,** A. M. C. Ng, *J. Mater. Chem.*, 2012, **22**, 6526; (c) C. Klingshirn, *ChemPhysChem*, 2007, **8**, 782.

2   (a) M. H. Huang, S. Mao, H. Feick, H. Yan, Y. Wu, H. Kind, E. Weber, R. Russo, P. Yang, *Science*, 2001, **292**, 1897; (b) J. C. Johnson, H. Yan, R. D. Schaller, L. H. Haber, R. J. Saykally, P. Yang, *J. Phys. Chem. B*, 2001, **105**, 11387.

3   S. Kumar, V. Gupta and K. Sreenivas, *Nanotechnology*, 2005, **16**, 1167.

4   (a) M. Law, L. E. Greene, J. C. Johnson, R. Saykally, P. Yang, *Nat. Mater.*, 2005, **4**, 455; (b) H. Rensmo, K. Keis, H. Lindstrom, S. Sodergren, A. Solbrand, A. Hagfeldt, S. E. Lindquist, L. N. Wang, M. Muhammed, *J. Phys. Chem. B,* 1997, **101**, 2598.

5   (a) L. Xu, Y.-L. Hu, C. Pelligra, C.-H. Chen, L. Jin, H. Huang, S. Sithambaram, M. Aindow, R. Joesten, S. L. Suib, *Chem. Mater.*, 2009, **21**, 2875; (b) B., Li, Y. Wang, *J. Phys. Chem. C*, 2010**, 114***,* 890.

6   (a) H. Hong, J. Shi, Y. Yang, Y. Zhang, J. W. Engle, R. J. Nickles, X. Wang, W. Cai, *Nano Lett.*, 2011, **11**, 3744; (b) A. V. Kachynski, A. N. Kuzmin, M. Nyk, I. Roy, P. N. Prasad, *J. Phys. Chem. C*, 2008, **112**, 10721; (c) H. M. Xiong, X. Yu, Q. G. Ren, Y. Y. Xia, *J. Am. Chem. Soc.*, 2008, **130**, 7522; (d) F. Guell, J. O. Osso, A. R. Goni, A. Cornet, J. R. Morante, *Nanotechnology*, 2009, **20**, 315701; (e) H. Wang, D. Wingett, M. H. Engelhard, K. Feris, K. M. Reddy, P. Turner, J. Layne, C. Hanley, J. Bell, D. Tenne, C. Wang, A. J. Punnoose, *Mater. Sci.: Mater. Med.*, 2009, **20**, 11; (f) H. Wang, H. Jiang, H. Zhang, Y. Zhou, C. Wu, J. Zhao, L. Ba, X. J. Wang, *Nanosci. Nanotechnol.*, 2011, **11**, 1117.

7   (a) R. Brayner, S. A. Dahoumane, C. Yéprémian, C. Djediat, M. Meyer, A. Couté, *Langmuir*, 2010, **26**, 6522; (b) J. W. Rasmussen, E. Martinez, P. Louka, D. G. Wingett, *Expert Opin Drug Deliv.*, 2010, **7**, 1063; (c) N. Tripathy, R. Ahmad, S. H. Bang, J. Min, Y.-B. Hahn, *Chem. Commun.*, 2014, **50**, 9298; (d) A. Lipovsky, Y. Nitzan, A. Gedanken, R. Lubart, *Nanotechnology*, 2011, **22**, 105101; (e) M. Li, S. Pokhrel, X. Jue, L. Mädler, R. Damoiseaux, E. M. V. Hoek, *Environ. Sci. Technol.*, 2011, **45**, 755.

8   (a) B. Ludi, M. Niederberger, *Dalton Trans.,* 2013, **42**, 12554; (b) E. S. Jang, J.-H. Won, S.-J.Hwang, J.-H. Choy, *Adv. Mater.*, 2006, **18**, 3309.

9   (a) J. Xu, Z. Chen, J. A. Zapien, C.-S. Lee, W. Zhang, *Adv. Mater.*, 2014, **26**, 5337; (b) Y. Liu, J. Goebl, Y. Yin, *Chem. Soc. Rev.*, 2013, **42**, 2610.

10 1D Structures. Nanowires: (a) J. G. Ok, S. H. Tawfick, K. A. Juggernauth, K. Sun, Y. Zhang, A. J. Hart, *Adv. Funct. Mater.*, 2010, **20**, 2740 (b) S. Xu, Y. Ding, Y. Wei, H. Fang, Y. Shen, A. K. Sood, D. L. Polla, Z. Lin Wang, *J. Am. Chem. Soc.,* 2009, **131**, 6670; (c) T. J. Hsueh, S. J. Chang, Y. R. Lin, S. Y. Tsai, I. C. Chen, C. L. Hsu, *Cryst. Growth Des.*, 2006, **6**, 1282; Nanotubes: (d) J. G. Ok, S. H. Tawfick, K. A. Juggernauth, K. Sun, Y. Zhang, A. John Hart, *Adv. Funct. Mater.*, 2010, **20**, 2470; Nanorods: (e) B. Liu, H. C. Zeng, *J. Am. Chem. Soc.*, 2003, **125**, 4430; (f) K. S. Kim, H. Jeong, M. S. Jeong, G. Y. Jung, *Adv. Funct. Mater.*, 2010, **20**, 3055; (g) J.-Y. Oh, J. Park,

S.-Y. Kang, C.-S. Hwang, H.-K. Shim, *Chem. Commun.*, 2009, 4545; Nanoneedles: (h) W. I Park, G.-C. Yi, M. Kim, S. J. Pennycook, *Adv. Mater.*, 2002, **14**, 1841; Nanoribbons: (i) X. Fan, M.-L. Zhang, I. Shafiq, W.-J. Zhang, *Adv. Mater.*, 2009, **21**, 2393; Nanobelts: (j) Y. B. Li, Y. Bando, T. Sato, K. Kurashima, *Appl. Phys. Lett.*, 2002, **81**, 144; (k) X. Y. Kong, Z. L. Wang, *Nano Lett.*, 2003, **3**, 1625; (l) X. Y. Kong, Z. L. Wang, *Science*, 2004, **303**, 1348; (m) J. B. Shen, H. Z. Zhuang, D. X. Wang, C. S. Xue, H. Liu, *Cryst. Growth Des.*, 2009, **9,** 2187.

11 2D strucutures Nanosheets: (a) Y. Zhang, J. Xu, Q. Xiang, H. Li, Q. Pan, P. Xu, *J. Phys. Chem. C*, 2009, **113**, 3430; (b) F. Lu, W. Cai, Y. Zhang, *Adv. Funct. Mater.*, 2008, **18**, 1047. Nanodisks: (c) F. Li, Y. Ding, P. X. Gao, X. Xin, Z. L. Wang *Angew. Chem. Int. Ed.*, 2004, **116**, 5350; (d) P. X. Gao, C. S. Lao, Y. Ding, Z. L. Wang, *Adv. Funct. Mater.*, 2006, **16**, 53; Nanoplates: (e) L. Wan, X. Wang, S. Yan, H. Yu, Z. Li, Z. Zou, *CrystEngComm*, 2012, **14**, 154; Nanowalls: Z. Liang, R. Gao, J.-L. Lan, O. Wiranwetchayan, Q. Zhang, C. Li, G. Cao in *Solar Energ. Mat. Sol. C.,* 2013**, 117**, 34.

12 3D structures. Spindle- and donut shaped: (a) A. Stan, C. Munteanu, A.M. Musuc, R. Birjega, R. Ene, A. Ianculescu, I. Raut, L. Jecu, M. Badea-Doni, E. M. Anghel, O. Carp, *Dalton Trans.*, 2015, **44**, 7844; (b) O. Carp, A. Tirsoaga, R. Ene, S. Somacescu, A. Ianculescu*, Carbohyd. Polym*., 2015, **111**, 285. Mushroom-like: (c) H. Wang, C. Xie, D. Zeng, Z. Yang, *J. Colloid Interf. Sci.*, 2006, **297**, 570; Hollow and solid spheres: (d) G. Patranoiu, J. M. Calderon-Moreno, R. Birjega, O. Carp, *RSC Adv.*, 2015, **5**, 31768. Bipyramids: (e) N. Wang, X. Cao, Q. Wu, R. Zhang, L. Wang, P. Yin, L. Guo, *J. Phys. Chem. C*, 2009, **113** , 21471; Tower-like: (f) Z. Wang, X. F. Qian, J. Yin, Z. K. Zhu, *Langmuir*, 2004, **20**, 3441. Flower-like: (g) N. Mir, M. Salavati-Niasaria, F. Davarc, *Chem. Eng. J.,* 2012, **181–182**, 779; (h) H. Zhang, R. Wu, Z. Chen, G. Liu, Z. Zhang, Z. Jiao, *CrystEngComm*, 2012, **14**, 1775.

13 M. Niederberger. G. Garnweitner, *Chem. Eur. J.*, 2006, **12**, 7282.

14 (a) D. Jézéquel, J. Guenot, N. Jouini, F. Fiévet, *J. Mater. Res.*, 1995, **10**, 77. (b) L. Poul, S. Ammar, N. Jouini, F. Fiévet, F. Villain, *J. Sol-Gel Sci. Techn.*, 2003, **26**, 261; (c) C. Feldmann, H.-O. Jungk, *Angew. Chem. Int. Ed.*, 2001, **40**, 359; (d) C. Li, Y. Zhao, L. Wang, G. Li, Z. Shi, S. H. Feng, *Eur. J. Inorg. Chem.*, 2010, 217; (e) X. S. Tang, E. S. G. Choo, L. Li, J. Ding, J. M. Xue, *Langmuir*, 2009, **25**, 5271; (f) M. Bitenc, P. Podbršček, Z. C. Orel, M. A. Cleveland, J. A. Paramo, R. M. Peters, Y. M. Strzhemechny, *Cryst. Growth Des.*, 2009, **9**, 997; (g) M. Bitenc, Goran Dražic, Z. C. Orel, *Cryst. Growth Des.*, 2009, **9**, 830.

15 (a) G. Ambrožič, S. Škapin, M. Žigon, Z. Crnjak Orel *J. Col. Interf. Sci.*, 2010, **346**, 317; (b) G. Ambrožič, S. Škapin, M. Žigon, Z. Crnjak Orel, *Mater. Res. Bull.*, 2011, **46**, 2497.

16 (a) I. R. Collins, S.E. Taylor, *J. Mater. Chem.*, 1992, **2**, 1277; (b) A. Anžlovar, K. Kogej, Z. Crnjak Orel, M. Žigon, *Express Polym. Lett.*, 2011, **7,** 604; (c) Z. H. Hu, G. Oskam, P. C. Searson, *J. Colloid Interface Sci.*, 2003, **263**, 454; (d) Z. S. Hu, G. Oskam, R. L. Penn, N. Pesika and P. C. Searson, *J. Phys. Chem. B*, 2003, **107**, 3124;

17 N. Saito, H. Haneda, *Sci. Technol. Adv. Mater.,* 2011, 064707.

18 (a) A. Dakhlaoui, M. Jendoubi, L. S. Smiri, A. Kanaev, N. Jouini, *J. Cryst. Growth*, 2009, **311**, 3989; (b) P. Zhu, J. Zhang, Z. Wu, Z. Zhang, *Cryst. Growth Des.,* 2008, **8,** 3148; (c) B. Liu, J. Xu, S. Ran, Z. Wang, D. Chen, G. Shen, *CrystEngComm*, 2012, **14**, 4582; (d) S. Lee, S. Jeong, D. Kim, S. Hwang, M. Jeon, J. Moon, *Superlattice Microstruct.*, 2008, **43**, 330; (e) Z. Jingwei, Z. Pengli, L. Zhiwei, C. Jianmin, W. Zhishen, Z. Zhijun, *Nanotechnology*, 2008, **19**, 165605; (f) N. Bouropoulos, I. Tsiaoussis, P. Poulopoulos, P. Roditis, S. Baskoutas, *Mater. Lett.* 2008, **62**, 3533; (g) S. Chen, B. Zhou, W. Hu, W. Zhang, N. Yin, H. Wang, *Carbohyd. Polym.* 2013*,* **92**, 1953.

RSC Advances Accepted Manuscript

19 (a) Z. Wang, C. Lin, X. Liu, G. Li, Y. Luo, Z. Quan, H. Xiang, J. Lin, *J. Phys. Chem. B*, 2006, **110***, 9469; (b) X. Hu, J. Gong, L. Zhang, J. C. Yu, *Adv. Mater.*, 2008, **20**, 4845; (c) K. Matsumoto, N. Saito, T. Mitate, J. Hojo, M. Inada, H. Haneda, *Cryst. Growth&Des.*, 2009, **9**, 5014; (d) A. Mclaren, T. Valdes-Solis, G. Li, S. C. Tsang, *J. Am. Chem. Soc.*, 2009, **131**, 12540; (e) P. Hu, X. Zhang, N. Han, W. Xiang, Y. Cao, F. Yuan, *Cryst. Growth Des.*, 2011, **11**, 1520; (f) A. Anžlovar, Z. Crnjak Orel, M. Žigon, *Eur. Polym. J.*, 2010, **46**, 1216; (g) N. Saito, H. Haneda, *Sci. Technol. Adv. Mater.*, 2011, **12**, 064707; (h) R. Brayner, S. A. Dahoumane, C. Yéprémian, C. Djediat, M. Meyer, A. Couté, *Langmuir*, 2010, **26**, 6522; (i) I. Trenque, S. Mornet, E. Duguet, M. Gaudon, *Inorg. Chem.*, 2013, **52**, 12811; (j) J. Rao, A. Yu, C. Shao, X. Zhou, *ACS Appl. Mater. Inter.*, 2012, **4**, 5346; (k) H. Dong, Y.-C. Chen and C. Feldmann, *Green Chem.,* 2015, **17**, 4107.

20 (a) M. G. Ma, J.-F. Zhu, J.-X. Jiang, R.-C. Sun, *Mat. Lett.*, 2009, **63**, 1791; (b) P. Prasertgdam, O. Mekasuwandumrong, J. Phungphadung, A. Kanyanucharat, *Cryst. Growth Des.*, 2003, **3**, 215; (c) S. Chaianansutcharit, O. Mekasuwandumrong, P. Prasertgdam, *Cryst. Growth Des.*, 2006, **6**, 40; (d) D. S. Bae, K.-S. Han, S.-B. Cho, S.-H. Choi, *Mat. Lett.*, 1998, **37**, 255; (e) J. Klongdee, W. Petchkroh, K. Phuempoonsathaporn, P. Prasertgdam, A. S. Vangai, V. Pavarajarn, *Sci. Technol. Adv. Mater.,* 2005, 6, 290; (e) M. Zawadzki, W. Walerczyk, F.E. López-Suárez, M. J. Illán Gómez, A. Bueno-López, *Catal. Commun.*, 2011, **12**, 1238; (f) Y. Zhang, M. E. Grass, S. E. Habas, F. Tao, T. Zhang, P. Yang, G. A. Somorjai, *J. Phys. Chem. C*, 2007, **111**, 12243.

21 (a) P. Prasertgdam, P. L. Silverston, O. Mekasuwandumrong, V. Pavarajan, J. Phungphdung, P. Somrang, *Cryst. Growth Des.*, 2004, **4**, 39; (b) K. D. Bhatte, P. Tambade, S.-i. Fujita, M. Arai, B. M. Bhanage, *Powder Technol.*, 2010, 415; (c) K. D. Bhatte, S.-i. Fujita, M. Arai, A. B. Pandit, B. M. Bhanage, *Ultrason. Sonochem.*, 2011, **18**, 54; (d) N. S. Bell, D. R. Tallamt, *J Sol-Gel Sci. Technol.*, 2009, **51**, 158; (e) M. Rezapoura, N. Talebian, *Mat. Chem. Phys.*, 2011, **129**, 249.

22 A. M. Grumezescu, E. Andronescu, A. Ficai, C. Bleotu, D. E. Mihaiescu, M. C. Chifiriuc, *Int. J. Pharmaceut.*, 2012, **436**, 771.

23 M. Bitenc, Z. Crnjak Orel, *Mater. Res. Bull.*, 2009, **44**, 381.

24 (a) L. Poul, N. Jouini, F. Fiévet, *Chem. Mater.*, 2000, **12**, 3123; (b) V. Prevot, C. Forano, and J. P. Besse, *Chem. Mater.*, 2005, **17***, 6695; (c) M. Taibi, S. Ammar, F. Schoenstein, N. Jouini, F. Fiévet, T. Chauveau, J.M. Greneche, *J. Phys. Chem. Solids*, 2008, **69**, 1052

25 R. Lin, P. Zhang, *J. Cryst. Growth*, 2002, **245**, 309.

26 J. C. Groen, L.A. Peffer, J. Perez-Rremirez, *Micropor. Mesopor. Mater.* 2003, **60**, 1.

27 K.C. Barick, Sarika Singh, M. Aslam, D. Bahadur, *Micropor. Mesopor. Mater.* 2010, **134**, 195.

28 T. Sahoo, M. Kim, J. H. Baek, S.-R. Jeon, J. S. Kim, Y. T. Yu, C.-R. Lee, I.-H. Lee, *Mater. Res. Bull.,* 2011, **46**, 525.

29 S. Dutta, S. Chattopadhyay, M. Sutradhar, A. Sarkar, M. Chakrabarti, D. Sanyal D. Jana*, J. Phys.: Condens. Mater.*, 2007*, 19*, 236218.

30 (a) S. T. Tan, B. J. Chen, X. W. Sun, W. J. Fan, H. S. Kwok, X. H. Zhang and S. J. Chua, *J. Appl. Phys.*, 2005, **98**, 13505; (b) V. Srikant and D. R. Clarke, *J. Appl. Phys.*, 1998, **83**, 5447.

31 (a) J. Tauc, R. Grigorovici, A. Vancu, *Phys. Status Solidi A*, 1966, **15**, 627; (b) I. Seguy, P. Jolinat, P. Destruel, J. Farence, R. Many, H. Bock, J. Ip, T. P. Nguyen, *J. Appl. Phys.*, 2001, **89**, 5442.

32 L. E. Greene, M. Law, J. Goldberger, F. Kim, J. C. Johnson, Y. Zhang, R. J. Saykally, P. D. Yang, *Angew. Chem. Int. Ed.*, 2003, **42**, 3031.

33 (a) A. B. Djurišić, Y. H. Leung, *Small*, 2006, **2**, 944; (b) V. A. Dijken, E. Meulenkamp, D. Vanmaekelbergh, A. Meijerink, *J.*

Phys. Chem. B, 2000, **104**, 1715; (c) J. Reeja, *J. Phys. Chem. C*, 2008, **112**, 240; (d) H. Xiong, Y. Xu, Q. Ren, Y. Xia, *J. Am. Chem. Soc.*, 2008, **130**, 7522.

34 (a) M. Ahmad, J. Zhu, *J. Mater. Chem.*, **2011**, *21*, 599; (b) F. Liu, P. J. Cao, H. R. Zhang, C. M. Shen, Z. Wang, J. Q. Li, H.J. Gao, *J. Cryst. Growth*, 2005, **274**, 126.

35 (a) H. B. Zeng, G. T. Duan, Y. Li, S. K. Yang, X. X. Xu, W. P. Cai, *Adv. Funct. Mater.*, 2010, **20**, 561; (b) X. L. Wu, G. G. Siu, C. L. Fu, H. C. Ong, *Appl. Phys. Lett.*, 2001, **78**, 2285; (c) B. Lin, Z. Fu, Y. Jia, *Appl. Phys. Lett.*, 2001, **79**, 943; (c) L. Jia, W. Cai, H. Wang, H. Zeng, *Cryst. Growth Des.*, 2008, **8**, 4367.

36 (a) M. L. Kahn, T. Cardinal, B. Bousquet, M. Monge, V. Jubera, B. Chaudret, *Chem. Phys. Chem.*, 2006, **7**, 2392; (b) H. Xiong, Z. Wang, Y. Xia, *Adv. Mater.*, 2006, **18**, 748.

37 Y. W. Heo, D. P. Norton, S. J. Pearton, *J. Appl. Phys.*, 2005, **98**, 073502.

38 (a) F. Wen, W. Li, J.-H. Moon, J.-H. Kim, *Solid State Commun.*, 2005, **135**, 34; (b) D. Li, Y. H. Leung, A. B. Djurišić, Z. T. Liu, M. H. Xie, S. L. Xie, S. L. Shi, S. J. Xu, W. K. Chan, *Appl. Phys. Lett.*, 2004, **85**, 1601.

39 C. Minero, *Catal. Today*, 2001, **67**, 273.

40 F. T. Wakida, D. N. Lerner, *Water Res.*, 2005, **39**, 3.

41 (a) K. T. Ranjit, B. Viswanathan, *J. Photoch. Photobio. A: Chemistry*, 1997, **108**, 73; (b) B. Ohtani, M. Kakimoto, H. Miyadzu, S. Nishimoto, T. Kagiya, *J. Phys. Chem.*, 1988, **92**, 5773; (c) F. Zhang, R. Jin, J. Chen, C. Shao, W. Gao, L. Li, N. Guan, *J. Catal.*, 2005, **232**, 424; (d) H. Kato, A. Kudo, *Phys. Chem. Chem. Phys.*, 2002, **4**, 2833; (e) M. Adachi, A. Kudo, *Chem. Lett.*, 2012, **41** 1007; (f) J. Sá, C. A. Agüera, S. Gross, J. A. Anderson, *Appl. Catal. B*, 2009, **85**, 192; (g) W. Gao, R. Jin, J. Chen, X. Guan, H. Zeng, F. Zhang, N. Guan, *Catal. Today*, 2004, **90**, 331; (h) L. Li, Z. Xu, F. Liu, Y. Shao, J. Wang, H. Wan, S. Zheng, *J. Photoch. Photobio. A: Chemistry*, 2010, **212**, 113; (i) H. Kominami, T. Nakaseko, Y. Shimada, A. Furusho, H. Inoue, S. Murakami, Y. Kera0, B. Ohtani, *Chem. Commun.*, 2005, 2933; (j) N. Wehbe, M. Jaafar, C. Guillard, J.M. Herrmann, S. Miachon, E. Puzenat, N.Guilhaume, *Appl. Cat. A: Gen.*, 2009, **368**, 1; (k) J. Hirayama, H. Kondo, Y. Miura, R. Abe, Y. Kamiya, *Catal. Commun.*, 2012, **20**, 99.

42 (a) B. Bems, F.C. Jentoft, R. Schlogl, *Appl. Catal. B: Environ.*, 1999, **20**, 155; (b) T. Mori, J. Suzuki, K. Fujimoto, M. Watanabe, Y. Hasegawa, *Appl. Catal. B: Environ.*, 1999, **23**, 283; (c) H. Kominami, T. Nakaseko, Y. Shimada, A. Furusho, H. Inoue, S. Murakami, Y. Kera, B. Ohtani, *Chem. Commun.*, 2005, 2933; (d) Y. Li, F. Wasgéstian, *J. Photoch. Photobio. A: Chemistry*, 1998, **112** 255.

43 M. Kaneko, I. Okura in *Photocatalysis. Science and Technology*, Eds., Kodansha Springer, 2002, p. 81

44 J.-M. Herrman, *Catal. Today*, 1999, **53**, 115.

45 K. Doudrick, T. Yang, K. Hristovski, P. Westerhoff, *Appl. Catal. B*, 2013, **136-137**, 40.

46 P. G. Luo, T. R. Tzeng, R. R. Shah, F. J. Stutzenberger, *Curr Trends Microbiol.* 2007, **3**,111.

47 (a) R. Wahab, A. Mishra, S.-I. Yun, Y.-S. Kim, H.-S. Shin, *Appl. Microbiol Biotechnol.*, 2010, **87**, 1917; (b) S. W. Kim, Y.-J. An, *Appl. Microbiol. Biotechnol.*, 2012, **95**, 243; (c) R. Sinha, R. Karan, A. Sinha, S.K. Khare, *Bioresource Technol.* 2011, **102**, 1516; (d) K. Kasemets, A. Ivask, H.-C. Dubourguier, A. Kahru, *Toxicol. in Vitro*, 2009, **23**, 1116; (e) J. Sawai, H. Igarashi, A. Hashimoto, T. Kokugan, M. Shimizu, *J. Chem. Eng. Jpn.,* 1996, **29**, 251; (f) S. Nair, A. Sasidharan, R.W. Divya, D. Menon, S. Nair, K. Manzoor, S. Raina, *J. Mater. Sci. Mater. Med.*, 2009, **20**, S235; (g) J. Sawai, E. Kawada, F. Kanou, H. Igarashi, A. Hashimoto, T. Kokugan, M. Shimizu, *J. Chem. Eng. Jpn.*, 1996, **29**, 627; (h) R. K. Dutta, B. P. Nenavathu, M. K. Gangishetty, A. V. R. Reddy, *Colloids Surf.*, 2012, **B 93**, 8; (i) J. Sawai, K. Hiromitsu, I. Hideo, H. Atsushi, S. Shinobu, T. Akemi, S. Takashi, K. Takao, S. Masaru, *J. Chem. Eng. Jpn.*, 1997, **30**,

1034; (j) J. Sawai, S. Shinobu, I. Hideo, H. Atsushi, K. Takao, S. Masaru, K. Hiromitsu, *J. Ferment. Bioeng.*, 1998, **86**, 521; (k) Y. Zhihong, X. Changsheng, *Colloids Surf.*, 2006, **B 47**, 140; (l) Z. Lingling, J. Yunhong, D. Yulong, P. Malcom, Y. David, *J. Nanopart. Res*., 2007, **9**, 479; (m) L. K. Adams, D. Y. Lyon, P. J. Alvarez, *Water Res.*, 2006, **40**, 3527; (n) K. M. Reddy, F. Kevin, B. Jason, G. W. Denise, H. Cory, P. Alex, *Appl. Phys. Lett.*, 2007, **90**, 213902.

48 A. V. Kirthi, A. A. Rahuman, G. Rajakumar, S. Marimuthu, T. Santhoshkumar, C. Jayaseelan, K. Velayutham, *Parasitol. Res.*, 2011, **109**, 461.

49 N. L. Rosi, C. A. Mirkin, *Chem. Rev.*, 2005, **105**, 1547.

50 (a) K. Feris, C. Otto, J. Tinker, D. Wingett, A. Punnoose, A. Thurber, M. Kongara, M. Sabetian, B. Quinn, C. Hanna, D. Pink, *Langmuir*, 2010, **26**, 4429; (b) G. M. Teitzel, A. Geddie, S. K. De Long, M. J. Kirisits, M. Whiteley, M. R. Parsek, *J. Bacteriol.*, 2006, **188**, 7242; (c) J. J. Harrison, H. Ceri, C. A. Stremick, R. J. Turner, *Environ. Microbiol.*, 2004, **6**, 1220; (d) M. Premanathan, Kr.Karthikeyan, K. Jeyasubramanian, G. Manivannan, *Nanomed.-Nanotechnol.*, 2011, **7**, 184.

51 I. Matai, A. Sachdev, P. Dubey, S. Uday Kumar, B. Bhushan, P. Gopinath, *Colloid. Surface B*, 2014, **115**, 359.

52 (a) Y. A. Xu, , D. Fu, C. Yuan, *Appl. Surf. Sci.*, 2008, **254**, 3033; (b) M. Fang, J. H. Chen, X. L. Xu, P. H. Yang, H. F. Hildebrand, *Inter. J. Antimicrob. Agents*, 2006, **27**, 513; (c) N. Sharma, J. Kumar, S. Thakur, S. Sharma, V. Shrivastava, *Drug Invention Today*, 2013, **5**, 50; (d) N. Jones, B. Ray, K. T. Ranjit, A. C. Manna, *FEMS Microbiology Letters*, 2007, 279.

53 (a) M. Eshed, J. Lellouche, S. Matalon, A. Gedanken, E. Banin, *Langmuir*, 2012, **28**, 12288; (b) A. Shrestha, Z. Shi, K. G. Neoh, A. Kishen, *J. Endod.*, 2010, **36**, 1030; (c) N. Hoiby, T. Bjarnsholt, M. Givskov, S. Molin, O. Ciofu, *Int. J. Antimicrob. Agents*, 2010, **35**, 322; (d) J. W. Costerton, P. S. Stewart, E. P. Greenberg, *Science*, 1999, **284**, 1318; (e) I. W. Sutherland in *Bacterial exopolysaccharides – their nature and production, in: Surface Carbohydrates of the Prokaryotic Cell*, Ed. Academic, London, 1977, pp. 27–96.

54 M. Shafiei, A. A. Ali, F. Shahcheraghi, A. Saboora, K. A. Noghabi, *Jundishapur J. Microbiol.*, 2014, **7,** e14358